Universidad de Cantabria

Departamento de Física Moderna

CSIC - Universidad de Cantabria

Instituto de Física de Cantabria

Detection of Point Sources in Maps of the Cosmic Microwave Background Radiation by means of Optimal Filters

A dissertation submited in partial of the requirements

for the degree of Doctor of Philosophy in Physics

by

Marcos López-Caniego Alcarria

2006

CHAPTER 6

Planck simulations: flat patch approximation

We study the detection of extragalactic point sources in two-dimensional flat simulations for all the frequencies of the forthcoming ESA's Planck mission. In this work we have used the most recent available templates of the microwave sky: as for the diffuse Galactic components and the Sunyaev-Zel'dovich clusters we have used the "Plank Reference Sky Model"; as for the extragalactic point sources, our simulations - which comprise all the source populations relevant in this frequency interval - are based on up-to-date cosmological evolution models for sources. To consistently compare the capabilities of different filters for the compilation of the - hopefully - most complete blind catalogue of point sources, we have obtained three catalogues by filtering the simulated sky maps with: the Matched Filter (MF), the Mexican Hat Wavelet (MHW1) and the Mexican Hat Wavelet 2 (MHW2), the first two members of the MHW Family. For the nine Planck frequencies we show the number of real and spurious detections and the percentage of spurious detections at different flux detection limits as well as the completeness level of the catalogues and the average errors in the estimation of the flux density of detected sources. Allowing a 5% os spurious detections, we obtain the following number of detections by filtering with the MHW2 an area equivalent to half of the sky: 580 (30 GHz), 342 (44 GHz), 341 (70 GHz), 730 (100 GHz), 1130 (143 GHz), 1233 (217 GHz), 990 (353 GHz), 1025 (545 GHz) and 3183 (857 GHz). Our current results indicate that the MF and the MHW2 yield similar results, whereas the MHW1 performs worse in some cases and especially at very low fluxes. This is a relevant result, because we are able to obtain comparable results with the well known Matched

Filter and with this specific wavelet, the MHW2, which is much easier to implement and use, see López-Caniego et al. [90].

6.1 Introduction

In two years from now, the ESA's Planck[1] satellite [137] will inaugurate a new era in the studies of the Cosmic Microwave Background (CMB) radiation. Planck will observe the microwave sky with unprecedented angular resolution and sensitivity in nine frequency channels ranging from 30 to 857 GHz. Besides CMB anisotropies, Planck will also yield all-sky maps of all the major sources of microwave emission, including a large number of extragalactic sources that have not yet been observed at these frequencies. The study of these sources of microwave emission –often referred to as *"contaminants"* or *"foregrounds"*– is twofold: on one hand, it is necessary to remove them in order to have the cleanest possible view of the CMB and, on the other hand, a better knowledge of the different foregrounds is a scientific goal in itself. As the launch date approaches, a big effort is being made to develop and to test state-of-the-art data processing techniques that will optimise the scientific exploitation of the forthcoming Planck data.

The case of extragalactic foregrounds deserves to be considered in detail. Radio and infrared selected galaxies will be seen by Planck as point-like objects due to their very small projected angular size as compared to the experiment resolution (see Table 1). Hence, they are usually referred to as extragalactic point sources or just as *point sources* (as we do hereafter). Point sources are expected to be a major contaminant for Planck at multipoles $\ell \geq 500 - 1000$ [31, 75, 140, 141] and it is necessary to detect and remove as many of them as possible in order to clean CMB maps. As a very important astrophysics by-product, the detection process will yield all-sky catalogues of extragalactic point sources in a frequency interval in which they are lacking and that will prove very useful to constrain models of galaxy formation and evolution.

Unfortunately, many of the component separation techniques that are generally used to separate diffuse Galactic foregrounds are not well suited to deal with point sources. This is mainly due to the fact that each galaxy is an independent source, different, in principle, to any other source in the sky. Albeit average energy spectra can be defined for different source populations, the spectral emission law is different for each galaxy and it makes impossible to apply separation methods which exploits a single energy spectrum for this foreground component.

[1] http://www.rssd.esa.int/index.php?project=Planck

If the lack of knowledge on their spectral emission properties can be troublesome, their projected angular shape is basically the same for all of them: a Dirac's δ-like response convolved with the instrument beam response function. Thus, techniques that take into account the specific angular shape of point sources, such as wavelets and band-pass filters, are particularly useful for detecting them. In the last few years a number of techniques have been proposed for the specific case of point source detection in CMB maps, including the Mexican Hat Wavelet [19, 144, 145, 146], the Matched filter (MF) [139], the Scale-Adaptive filter [68, 69, 124], the Adaptive Top Hat filter [20], the Bi-parametric Scale-Adaptive filter [87] and the recently introduced Mexican Hat Wavelet Family [51]. All the previously mentioned methods belong to the class of wavelet and linear filter techniques. Additionally, non-linear techniques such as Bayesian detection [76] have been successfully applied to point source detection in the CMB context, but since the use of those techniques implies a totally different methodological approach we will focus on the above mentioned filters and wavelets. Whereas some works have made an effort to compare the performances of some of them both theoretically and by using almost-ideal simulations [5, 87, 148], an attempt to compare the existent techniques under *(almost)* "real life" conditions for the future Planck mission has not been done, yet.

In this work we intend to reproduce the conditions of a blind point source survey as it will be carried out by Planck. We will use the Planck Reference Sky and the nominal Planck instrument characteristics and goal performance to simulate realistic sky emission as it should be observed at the nine frequencies covered by the satellite. Using such realistic simulations we will compare the performance of different filters. The ultimate goal is to decide which is the best tool of choice for the Planck case. The 'goodness' of a filter will be evaluated according to the following criteria:

(i) The filter must be well suited to conduct a blind survey, that is, it must be able to work well with a minimum number of a priori assumptions about the data.

(ii) Besides, it must be robust against the effect of possible systematics.

(iii) It must yield, after the detection process, a high number of positive detections.

(iv) It must yield, after the detection process, a low number of false detections (not higher that, let us say, 5% of the integral, or total, number of detections above the corresponding detection threshold).

(v) Moreover, additional factors, such as the flux detection limit of the output catalogue, its completeness and the accuracy with which the positions and the flux densities of the sources are estimated, will be taken into account.

We would like to remind that previous criteria are similar to those required for the Early Release Compact Source Catalogue, ERCSC, a blind catalogue of point sources that is one of the objectives of the Planck collaboration. In the compilation of this kind of catalogue, factors such as quickness and accuracy of the estimation of the flux of the sources have the priority over a high absolute number of detections. Keeping this in mind, criterion 1 eliminates from the competition tools such as the Biparametric Scale-Adaptive filter that, even if they are potentially very powerful, require a detailed knowledge of the probability distribution of the foregrounds[2]. The Adaptive Top Hat filter is known to produce strong ringing artifacts around the sources which can lead to a high number of false detections –against criterion 4–, in particular in the vicinity of bright sources. The Scale-Adaptive filter seems to perform similarly or slightly worse than the MF [70]. Therefore, in this work we will focus on the comparison of two tools: the Mexican Hat Wavelet Family (MHWF), which includes the standard Mexican Hat Wavelet, and the Matched Filter[3].

At first glance, the MF should be the obvious winner in the comparison. By definition, it is the best linear operator that can be applied to the data in order to maximise the signal to noise ratio of a signal with a known profile embedded in additive noise. But, in practise, the use of MFs does not lack of subtleties that must be considered here.

In Fourier space the MF is proportional to the inverse of the power spectrum of the noise. That means that the power spectrum of the noise must either be known a priori or be estimated from the data in order to construct the filter. If point sources are scarce, the power spectrum of the noise can be reasonably approximated by the power spectrum of the observed data, that is easy to *estimate* by means of any of the power spectra toolboxes available in scientific softwares. But any estimated power spectrum, as good as it may be, is just a good guess of the real thing. This leads to a number of problems:

- Firstly, it is necessary to estimate the value of the power spectrum for all the Fourier modes present in the image. This implies the estimation of several hundreds of numbers for a typical CMB image. For the typical image size of the sky patches we work with, each Fourier mode must be estimated from a small number of data samples. Therefore, the estimated power spectrum is *noisy*, especially at low Fourier modes. On the contrary, to use the various members of the

[2]Such tools could be very useful for exhaustive data mining the sky down to very low flux limits.

[3]In particular, González-Nuevo et al. [51] have shown that the second member of the Mexican Hat Wavelet Family (to be introduced in section 6.2) is the one that gives the best results for the case of the Planck Low Frequency Instrument (LFI) channels, and therefore we will limit the discussion to this wavelet, comparing it with the standard Mexican Hat (the first member of the family), that has been widely used in the literature with good results, and the matched filter.

Mexican Hat Wavelet Family it is only necessary to determine one single number, the optimal scale of the wavelet and, thus, it is much less sensitive to noise estimation.

- Since the estimated power spectrum is noisy, if it is directly used to construct the MF it very often happens that the resulting filter is so full of discontinuities and 'jumps' in Fourier space that strong ringing effects appear in the filtered image. Therefore, it is necessary to smooth the power spectrum before constructing the filter. The different possible choices used in the smoothing procedure introduce some degree of arbitrarity in the use of MFs: one can, for example, apply some binning and interpolation scheme, or use polynomial fitting to the power spectrum, etc.

- An additional problem appears when it is not possible to properly estimate some Fourier modes. This is the case when the image which has to be filtered is not complete (for example, if a mask is applied to the data in order to cut bad pixels, or in areas of the sky where there is incomplete coverage by the instrument). In that case the missing modes must be somehow guessed in order to build the MF. This problem is much less relevant for the case of wavelets.

- Moreover, if we make considerations in the sphere we will have to deal with important problems when using a Matched filter as compared with a wavelet. These problems arise from the fact that the foregrounds are very different in different regions of the sky and therefore we need to use the appropriate filter for every region. The approach followed by Vielva et al. [146] using the Spherical MHW (SMHW) was to divide the sky in a number N of regions and obtain the optimal scale for all of them. Then they determined that many of these scales gave similar results and that they could be divided in a small number of different groups. This allowed them to construct just a few filters in the sphere with their corresponding scales and filter the maps a small number of times instead of N. This is important because depending on the resolution, the filtering process may need a lot of CPU time. The problem with the MF is that instead of calculating N optimal scales we would need to calculate N filters, calculating the power spectra from the N regions, and filtering the maps N times, once for every filter. This process will require enormous amounts of CPU time, especially when dealing with high resolution images, and therefore will make it unfeasible in practise.

Therefore, and as any experienced practitioner perfectly knows, the use of the MF is not the same as filtering by the inverse of the squared Fourier transform of the data.

On the contrary, it requires a non negligible effort of handmade tuning that is not free from arbitrarities. Besides, all the previous effects lead to an unavoidable degradation of the performance of the MF under realistic conditions.

Furthermore, all the theoretical superiority of the MF with respect to other linear filters comes from the fact that it maximises the signal to noise ratio, that is, it minimises the variance of the filtered noise. But if the noise is not Gaussian, as it is the case in CMB maps due to the emission contributed by Galactic foregrounds, *the fact that the variance is minimum does not guarantee that the number of false detections be minimum*. There may be outliers that are not removed. In that case, it is not by any means clear that the MF should be better than any other filter.

Taking all the previous points into account, the comparison between the MF and the wavelets is still necessary. The performance of wavelets will degrade as well when going from ideal to realistic conditions. Wavelets, however, are much less sensitive than MFs to the problems described in the paragraphs above. Therefore, it is expected that the performance degradation will be less severe. If we can find a wavelet that performs nearly as well as the MF, but without having to resort to handmade tuning, we will have a detection tool that is as good as the MF regarding criteria 3, 4 and 5 but is better regarding criterion 1 and 2. Such a wavelet would be preferable to MF for the compilation of a Planck blind point source catalogue.

In Section 6.2 we briefly review the tools to be used in this work: the MF and the wavelets belonging to the Mexican Hat Wavelet Family. In Section 6.3 we describe the realistic Planck simulations we use. The results are summarised in Section 6.4. In Section 6.5 we discuss some additional issues regarding point source detection in microwave satellite missions. Finally, we describe our main conclusions in Section 6.6.

6.2 Methodology

In this Section we consider the detection of compact (point-like) sources where A is the intrinsic flux density of the source and $s(x) = A\tau(x)$ is the observed flux, filtered by a circular Gaussian profile $\tau(x) = \exp(-x^2/2R^2)$, $x = |\vec{x}|$, whose Fourier transform is $\tau(q) = R^2 \exp(-(qR)^2/2)$, $q \equiv |\vec{q}|$. Such profile represents a commonly used useful approximation to the real profile of the beam response function, which can be more complicated and not analytically simple to describe. Of course, the MF can be easily designed for a non-axysimmetric beam, but also elliptical extension of the MHWF can be done (for instance, the elliptical MHW has been used in McEwen et al. [102] and Cruz et al. [25]). In general, the elliptical approximation is good enough for the typical

beam shapes of the CMB experiments. In any case, dealing with non-axysimmetric tools implies increasing the CPU time, since different orientation must be considered. Fortunately, as it was shown by Vielva et al. [146], data with non-axysimmetric but well known main beams can be still analysed with isotropic filters by characterising the bias introduced for the particular beam shape.

Given the above, the filtered sources in the map appear as circularly symmetric objects and, with the assumption that the background is statistically homogeneous and isotropic, the most natural thing to do - for detecting point-like sources - is the application of circularly symmetric filters to the map. More specifically, let us consider a 2D filter $\Psi(\vec{x}; R, \vec{b})$, where R and $\vec{b}$ define a scaling and a translation respectively, then

$$\Psi(\vec{x}; R, \vec{b}) \equiv \frac{1}{R^2}\psi\left(\frac{|\vec{x}-\vec{b}|}{R}\right). \tag{6.2.1}$$

If we filter our field $f(\vec{x})$ with $\Psi(\vec{x}; R, \vec{b})$, the filtered map will be

$$w(R, \vec{b}) = \int d\vec{x}\, f(\vec{x})\Psi(\vec{x}; R, \vec{b}). \tag{6.2.2}$$

The filter is normalised such that the flux of the source in the position of the source ($b = \vec{0}$) is the same after filtering:

$$\int d\vec{x}\, \tau(\vec{x})\Psi(\vec{x}; R, \vec{0}) = 1. \tag{6.2.3}$$

For the filtered map the moment of order-n is defined as

$$\sigma_n^2 \equiv 2\pi \int_0^\infty dq\, q^{1+2n} P(q)\psi^2(q). \tag{6.2.4}$$

where $P(q)$ is the power spectrum of the unfiltered map. Note that the zeroth-order moment, σ_0, is the dispersion of the filtered map.

As a result, the source profile described above is characterised by the "natural scale" R. This parameter appears in all the filters that we will consider in the following. For a given "optimal scale", R_0, the amplification (A/σ_0) of the source flux has a maximum value. By working at this particular scale – at which a filter maximise the flux of a compact source with respect to the average surrounding background value – it is possible to significantly improve the performance of the chosen filter in terms of detecting compact objects [86, 87, 144, 146].

6.2.1 The Matched Filter (MF)

The MF can be obtained by introducing a circularly-symmetric filter, $\Psi(x; R, b)$, and imposing the following two conditions: (1) $\langle w(R_0, 0)\rangle = s(0) \equiv A$, i. e. $w(R, 0)$ is an

unbiased estimator of the flux density of the source; (2) the variance of $w(R,b)$ has a minimum at the scale R_0, i. e. it is an *efficient* estimator

$$\hat{\psi}_{MF} = \frac{1}{a}\frac{\tau(q)}{P(q)}, \quad a = 2\pi \int dq q \frac{\tau^2(q)}{P(q)}. \tag{6.2.5}$$

As mentioned in the previous section, the practical implementation of the MF requires some additional work. In equation (6.2.5) the source profile $\tau(q)$ is known, but the power spectrum $P(q)$ must be estimated from the data. Moreover, the normalisation a must be calculated by integrating $P(q)$. The estimation of the power spectrum from the data can be easily done, but the estimates are necessarily noisy. In our case we use flat patches with sizes varying from 128×128 to 512×512 pixels. For small patches like the ones we use, we obtain a extremely noisy power spectrum and we need to smooth it before it can be used. We have found that a smoothing procedure that consists in binning the power spectrum modes and performing linear interpolation for the power spectrum values lying between the bin centres works well. Our tests suggest that the results vary slightly for any number of bins between 25 and 50, but the performance degrades quickly outside this interval. As for the results discussed in this work, we bin the Fourier modes in 40 uniformly spaced bins. Even so, the filter that we construct is noisy, as seen in Figure 6.1. In this figure we have compared the three chosen filters at each Planck frequency and for one of the simulations: the MF and the first two members of the MHWF (that will be introduced in the next section). It is easy to appreciate that the resulting MF is very noisy if compared to the smooth curves of the two wavelets, that only depend on the optimal scale, a quantity which can be easily estimated (see below).

6.2.2 The Mexican Hat Wavelet Family

The Mexican Hat Wavelet Family (MHWF) has been discussed by González-Nuevo et al. [51] and it is the extension of the MHW, obtained by applying iteratively the Laplacian operator to the Gaussian function.

The Fourier transform of $\psi_n(x)$ is

$$\hat{\psi}_n(q) = \int_0^\infty dx\, x J_0(qx)\psi_n(x), \tag{6.2.6}$$

where $\vec{q}$ is the wave number, $q \equiv |\vec{q}|$ and J_0 is the Bessel function of the first kind. Any member of this family can be written in Fourier space as

$$\hat{\psi}_n(q) \propto q^{2n} e^{-\frac{q^2}{2}}. \tag{6.2.7}$$

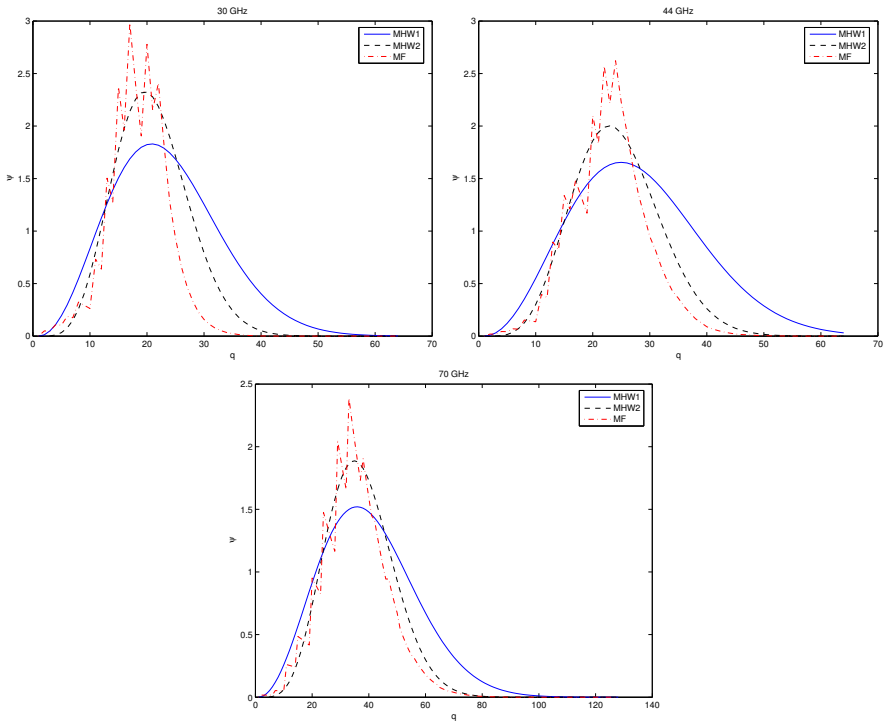

Figure 6.1 In each panel we compare the three chosen filters in Fourier space as they result at each Planck LFI frequency (30, 44 and 70 GHz) for one simulation. The solid line corresponds to the MHW1, the dashed line to the MHW2 and the dot-dashed one to the MF. The MHW1 and MHW2 operate at their optimal scale, a scale that yields the maximum average amplification of the source flux. The plots show that the MF is noisy as compared to the two adopted wavelets. As a remarkable result, we want to point out that the MF and the MHW2 have very similar behaviours in most of the plots.

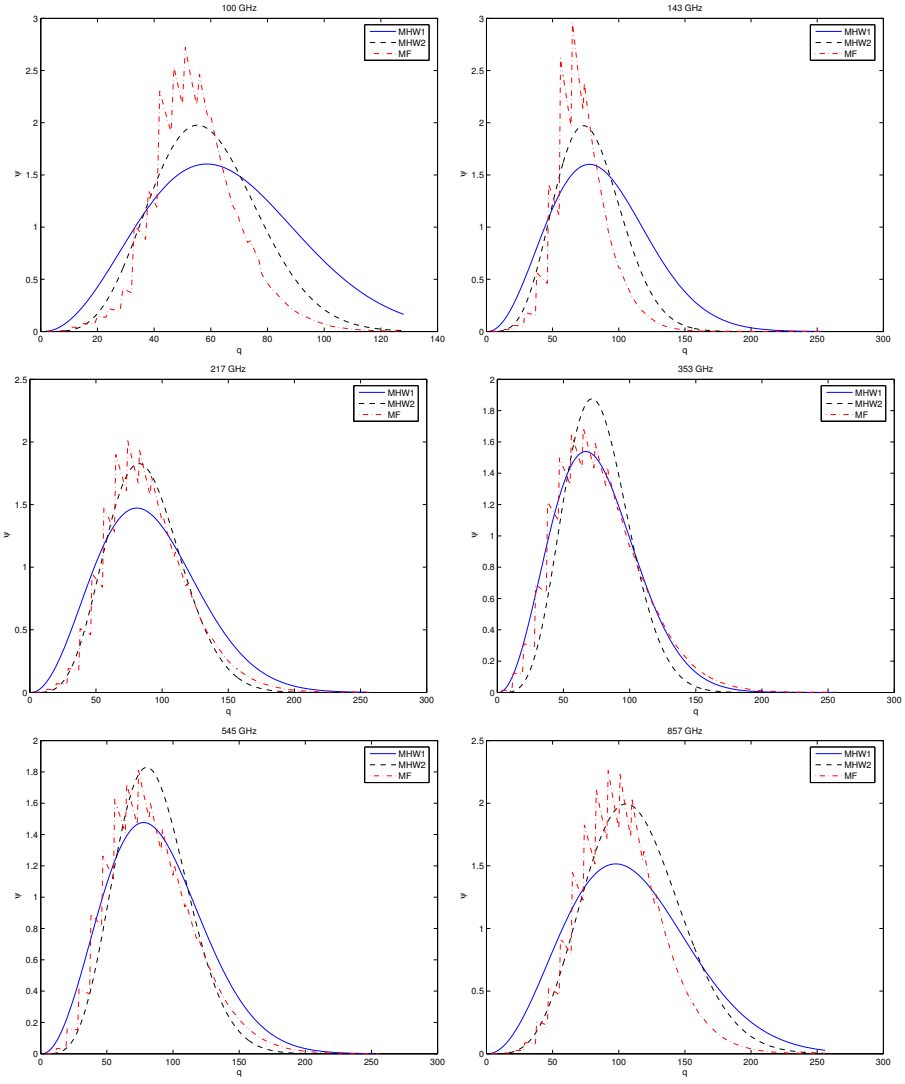

Figure 6.2 In each panel we compare the three chosen filters in Fourier space as they result at each Planck HFI frequency (199, 143, 217, 353, 545 and 857 GHZ) for one simulation. The solid line corresponds to the MHW1, the dashed line to the MHW2 and the dot-dashed one to the MF. The MHW1 and MHW2 operate at their optimal scale, a scale that yields the maximum average amplification of the source flux. The plots show that the MF is noisy as compared to the two adopted wavelets. As a remarkable result, we want to point out that the MF and the MHW2 have very similar behaviours in most of the plots.

The expression in real space for these wavelets is

$$\psi_n(x) \propto \triangle^n \varphi(x), \tag{6.2.8}$$

where φ is the 2D Gaussian $\varphi(x) = \frac{1}{2\pi} e^{-x^2/2}$.

Note that $\psi_1(x)$ is the usual MHW (hereinafter MHW1), a wavelet that has been extensively tested in the field of point detection with excellent results. Note that we call MHWn the member of the MHWF with index n.

The goal in the work by González-Nuevo et al. [51] was to compare the performance of some members of the MHWF and the main conclusion was that the second level wavelet $\psi_2(x)$ did perform better than $\psi_1(x)$ for the channels of the low frequency instrument of Planck.

In this work we are going to concentrate on these two wavelets, $\psi_1(x)$ and $\psi_2(x)$, and compare them with the Matched filter, as described in the previous subsection, for both the LFI and HFI channels.

Now let us consider a field $f(\vec{x})$ on the plane R^2, where $\vec{x}$ is an arbitrary point. One can define the wavelet coefficient at scale R at the point $\vec{b}$ in the form given by equations (6.2.1) and (6.2.2).

The wavelet coefficients $w_n(\vec{b}, R)$ for the members of the MHWF can be obtained in the following form

$$w_n(\vec{b}, R) = \int d\vec{q} e^{-i\vec{q}\cdot\vec{b}} f(\vec{q}) \hat{\psi}_n(qR), \tag{6.2.9}$$

assuming the appropriate differential and boundary conditions for the field this expression can be rewritten as

$$w_n(\vec{b}, R) \propto \int d\vec{x} \, [\triangle^n f(\vec{x})] \varphi\Big(\frac{|\vec{x} - \vec{b}|}{R}\Big). \tag{6.2.10}$$

and the wavelet coefficient at point $\vec{b}$ can be interpreted as the filtering by a Gaussian window of the invariant $(2n)^{th}$-order differences of the field f.

6.3 Simulations

We want to compare the capabilities of the MHW1, the MHW2 and of the MF when dealing with the detection of compact sources in realistic CMB maps.

To test these tools in the most realistic conditions so far, we used the latest "Planck Reference Sky Model" provided by the Working Group 2 (WG2, "Component separation")

of the Planck Consortium. All the available astrophysics foregrounds components are provided in all-sky maps in the HEALPix format [52] and include the following components:

- Thermal dust emission: has been created using a combination of two grey bodies with mean emissivity parameters $\alpha_1 = 1.67$ and $\alpha_2 = 2.70$ and mean temperatures $T_1 = 9.4K$ and $T_2 = 16.2K$ based on the Finkbeiner, Davis, & Schlegel [44] model.
- Synchrotron emission: is a cleaned version of the 408 GHz Haslam et al. [65] map made by Giardino et al. [49].
- Free-Free radiation: it adopts the free-free model of Dickinson, Davies, & Davis [38] which has been obtained by different $H\alpha$ surveys (e.g. WHAM [61], SHASSA [48]).
- S-Z Clusters: follow-up of the works by Colafrancesco et al. [22], De Zotti et al. [31, 32] and by P. Mazzotta.

As for point sources (not contained in the "Planck Reference Sky model", yet) we have used the simulation software (EPSS-2D) presented by González-Nuevo et al. [50] which is a very fast and efficient tool for simulating maps of extragalactic point sources. For this first comparison among the capabilities of different filters for source detection, we have adopted a simple Poisson distribution of point sources in the sky, not considering the clustering properties of the different source populations.

The input number counts are the ones foreseen by the De Zotti et al. [32] evolution model for radio-selected sources and by the Granato et al. [53, 54] model for high-z proto-spheroidal galaxies. These two models have proven very successful in fitting the observed source number counts recently obtained by the VSA, ATCA, WMAP and CBI surveys (at $\sim$15-30 GHz), and by the SCUBA and MAMBO surveys (in the far-IR/sub-mm domain), respectively. As for late-type far-IR galaxies we followed the same phenomenological approach as in Negrello et al. [104].

At each frequency, 145 patches of 12.8x12.8 square degrees have been simulated, covering a total effective area of 2π sr (half of the sky). Each patch has contribution from: a CMB realisation following the Concordance Model [132], a point source realisation given by the model described above and the sum of all the Galactic components. Galactic foregrounds have been selected from 12 different regions of the sky (at Galactic latitude $b > 30^\circ$). These 12 regions are representatives (in terms of its dispersion) of the Galactic emission outside the above mentioned Galactic cut. Each one of these 12

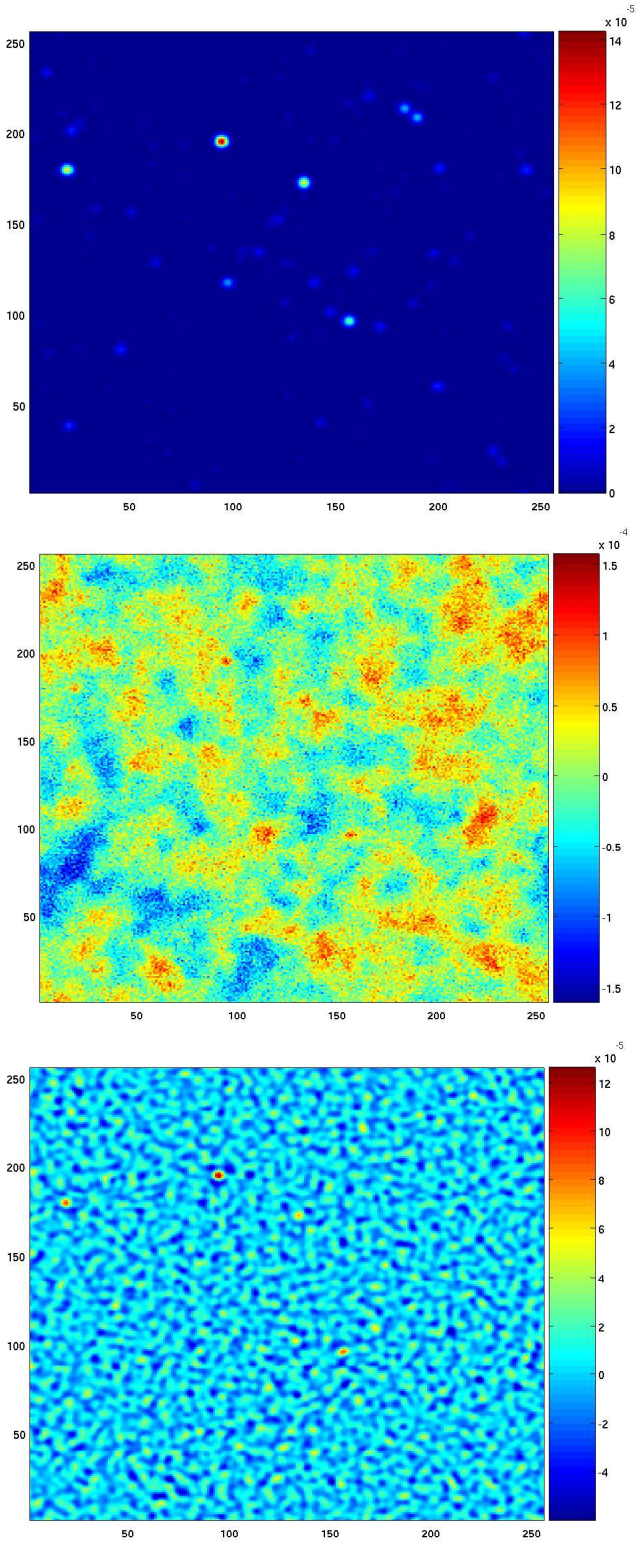

Figure 6.3 In this figure we show one of the simulations at 70 GHz. In the upper panel we show a simulation of point sources after they have been convolved with the beam of the instrument. In the middle and lower panels we have the the combination of the different components before and after filtering with the MHW2.

Galactic simulations has been used accordantly to their representativeness. This is a similar procedure to the one followed in Vielva et al. [144] (in that case 10 Galactic patches were considered).

Once the CMB, the point sources and the Galactic components have been added, the resultant map is convolved using the instrumental Planck specifications (see Table 6.1). Finally a Gaussian white noise realisation is added, with a dispersion per pixel according to the Planck specifications (see Table 1).

Each image is filtered with the MF, the MHW1 and the MHW2. To avoid spurious artifacts due to border effects, five pixels on the edge of the image have not been considered. The MHW1 and MHW2 operates at their respective optimal scales. This optimal scale can be easily obtained by filtering the image with a series of scales and by finding the particular scale that produces an image with maximum amplification. Note that this procedure does not affect the flux of the sources, since the filters are normalised in such a way, eq. (3), that the flux of the source is always preserved.

We then compare the list of source candidates (our recovered catalogue) with the reference (input) source catalogue, by trying to match the detected sources with the simulated ones. A source candidate is considered as a positive detection if it is found within a radius $r \leq \mathrm{FWHM}/2$ from the corresponding source in the reference catalogue. Only those objects in the candidate catalogue with a positive matching and with an error in the estimate of their flux density $\leq 100\%$ (with respect to the flux of the simulated source) are considered as real (positive) detections. Every other candidate source with flux above a fixed detection threshold in the filtered map (see Figures) is considered as a false or *spurious detection* and it has not been included in the final catalogue, corresponding to that particular Planck channel.

6.4 Results and discussion

In this Section we compare the performances of the filters described and discussed in the previous sections (MHW1, MHW2, MF).

In Figures 6.4 to 6.12 we present a number of relevant plots for all the Planck frequency channels. In the upper panels of each Figure we show the integral (or total) number of real and of spurious detections (left and right panels, respectively) above different flux detection limits in half of the sky (see captions for more details). It is easy to appreciate that the three filters detect approximately the same number of objects in all the Planck channels. As regards the spurious, or false, detections, the MF and the

Freq. (GHz)	Im. Size (pixels)	FWHM (arcmin)	Pix. Size (arcmin)	σ_{noise} (10^{-6})
857	512	5.0	1.5	6700.0
545	512	5.0	1.5	147.0
353	512	5.0	1.5	14.7
217	512	5.0	1.5	4.8
143	512	7.1	1.5	2.2
100	256	9.5	3.0	2.5
70	256	14.0	3.0	4.7
44	128	24.0	6.0	2.7
30	128	33.0	6.0	2.0

Table 6.1 Instrument performance goals for all the Planck satellite channels. The antenna is assumed to be a circular Gaussian one and the instrumental noise level is in units of $\Delta T/T$ per $FWHM$ (e.g in a square whose side is the FWHM of the beam).

MHW2 yield very similar results whereas the MHW1 detects a significantly higher number of spurious sources in comparison with the other two filters, in particular at frequencies $\leq$ 100 GHz and for faint flux detection limits.

In the lower left panels of Figures 6.4 to 6.12 we show the percentage of spurious detections with respect to the integral number of detections. These plots are very relevant ones because they compare the relative performance of the filters when taking into account both the number of real and of spurious detections. By these plots we can also establish the flux detection limit above which it is possible to reach a given percentage of spurious, e.g. 5%. It can also be noted that the behavior of the MF and the MHW2 is always comparable, whereas the MHW1 give worse results than these two filters at higher frequencies. At the lowest frequencies of the Planck experiment the MHW1 detects a relative higher number of spurious sources, but only when going down to faint flux detection thresholds.

In the lower right panels we also plot the completeness level of the catalogue above different flux detection thresholds. Each flux threshold represents the flux at which we have detected a given percentage (e.g., 95%, 100%) of all the simulated sources in the map. At low and intermediate Planck frequencies we find that our catalogues are 95% complete (the 95% of the simulated sources are detected above this flux limit) above $\simeq (300 - 350)$ mJy whereas at the highest Planck frequency, 857 GHz, the 95% completeness level is obtained only for fluxes $\geq$ 550 mJy. In Table 6.2 we have summarised these results for each Planck frequency channel and we have also included the 100%

completeness level, the flux limit at which all the simulated point sources are detected.

In Figure 6.13 we have plotted, for each Planck channel, the number of spurious detections against the number of real detections. This kind of representation, together with the plot of the percentage of spurious detections (in the lower left panels of Figures 6.4 to 6.12), is very important because it shows the global performance of the filters. It is clear that, for a given number of spurious detections, the filter which is able to obtain the corresponding highest number of real detected sources should be considered the best one. In this scheme, a filter performs better than another if its curve tends to lie above the other ones. In the upper panels of the Figure (i.e., at low Planck frequencies) we observe that the MF and the MHW2 behave similarly and better than MHW1, whose curve is always below the other two. At intermediate frequencies the three filters here discussed perform similarly, and at 217 GHz and 353 GHz the MHW1 curve is very close to those representing the MF and the MHW2. At 857 GHz, the curve representative of the MHW1 is again below the other two ones, but only at fluxes above $\simeq$ 650 mJy.

In Figure 6.15 we represent the average error in the estimate of the flux of the detected sources above different flux detection limits, and this error is defined as $< (A_{est} - A_{real})/A_{real} >$. This average error can take up negative values and instead of including the standard deviation we have plotted the true 68% error bars taking into account the probability distribution.

As expected, the error bars decrease towards higher fluxes. In Figure 6.15 it can be seen that there is a positive bias in the estimation of the flux. Such bias is negligible for high fluxes and increases towards lower fluxes. The bias is due to the well-known selection effect that makes more likely to detect a source when it is located on a positive fluctuation of the background, leading to a greater number of overestimated fluxes than the number of subestimated fluxes. This can also be appreciated in the non-symmetric shape of the observed error bars.

In Figure 6.17 we have represented the average distance between the position of the detected sources and their actual position in the simulated map before filtering. We have experienced that in some cases, after filtering, the maximum of a detected source has moved to an adjacent pixel. This fact would normally not affect our results, when matching candidate objects with the reference catalogues, because of the way we compare the simulated (input) and recovered (detected) sources (allowing a radius of $\leq$ FWHM/2 for the proper matching). In any case, in order to quantify this effect, we have calculated this distance for every detected source in each map. We have found that, even in the worst cases and only at very low Planck frequencies (i.e., 30, 44 GHz),

the average distance is always smaller than one pixel.

As for the MHW1, we have also checked to what extent a multi-fit approximation for estimating the source flux (i.e. a χ^2 fit of the wavelet coefficients to four scales $0.5, 1, 2$ and 3 times the optimal scale) can improve the number of real detections, as discussed in previous works on the same subject [144, 145, 146]. At frequencies above 100 GHz, the percentage of spurious detections with this wavelet decreases to the level of the MHW2, and at 857 GHz they are quite similar. On the other hand, at Planck frequencies below 100 GHz (LFI), while we still find a small improvement in comparison with the results previously plotted, the percentage of spurious detections does not reach the level of the MHW2, which performs always better.

As a final comment, it is clear that the multi-fit approximation only improves the estimation of the source fluxes at the highest frequencies and, correspondingly, reduces the number of the spurious detections. However, only at 857 GHz the performance of the MHW1 – with this method – is similar to that of the MHW2. As for the error in the estimated flux of the detected sources, we found that this method applied to the MHW1 yields estimated errors similar to those determined for the other filters.

6.5 Further details on the detection of point sources

In this section we briefly discuss some additional issues related to point source detection.

6.5.1 Confused/blended extragalactic point sources

Every time we observe the sky with a pencil- or a synthesised beam, if two or more point-like sources (i.e., distant galaxies or clusters) lay inside the beam area they appear as indistinguishable since they "blend" into a single source: a single "spot" in the map having the same angular dimension (FWHM) of the beam. As a result, only one “source” – whose flux is the integrated value of all the individual sources in the beam – is actually detected. However, if source counts are not very steep [30], this integrated flux value is mainly determined by the brightest source in the beam, whereas the much more numerous faintest sources are only slightly modifying the total flux and adding some noise [3, 47]. Thus, source blending is unlikely to affect the counts of bright sources, which are the ones actually detected.

As an example, at 30 GHz, if we reach the flux detection limit at which we have 5% of false detections, ~ 0.4 Jy, we have less than 0.007 sources per beam area and, thus,

Freq [GHz]	Filter	N_{d_5}	N_{sp_5}	S_5 [mJy]	SNR_5	A_{err} (%)	$N_{d_{95}}$	S_{95} [mJy]	$N_{d_{100}}$	S_{100} [mJy]
30	**MHW1**	497	26	448	3.79	12	583	329	327	545
	MHW2	580	30	391	3.75	12	595	324	432	447
	MF	594	31	382	3.63	10	594	324	432	447
44	**MHW1**	284	16	505	4.10	12	388	369	263	495
	MHW2	342	18	443	3.99	12	399	361	263	495
	MF	335	17	448	4.07	10	418	349	303	447
70	**MHW1**	304	16	510	4.59	8	445	339	276	495
	MHW2	341	18	473	4.54	9	444	339	276	495
	MF	344	18	467	4.49	9	443	339	276	495
100	**MHW1**	586	30	294	4.45	6	1237	138	871	198
	MHW2	730	38	248	4.42	7	1323	131	877	197
	MF	690	36	252	4.66	6	1325	131	877	197
143	**MHW1**	914	48	240	4.80	7	1713	116	1048	195
	MHW2	1130	59	196	4.73	7	1797	109	1049	195
	MF	829	43	250	6.25	2	1714	116	1049	195
217	**MHW1**	1153	61	195	4.87	6	1756	121	1074	195
	MHW2	1233	65	185	5.11	5	1755	121	1074	195
	MF	1242	65	195	5.57	3	1755	121	1074	195
353	**MHW1**	887	47	314	5.29	5	2253	147	1161	245
	MHW2	990	52	292	4.86	0	2243	147	1160	245
	MF	986	52	292	4.99	0	2247	147	1160	245
545	**MHW1**	726	38	785	6.33	8	2582	349	1495	495
	MHW2	1025	54	647	5.09	9	2568	349	1495	495
	MF	924	49	684	5.60	9	2580	349	1495	495
857	**MHW1**	1034	54	1765	8.24	2	13885	532	5194	745
	MHW2	3183	167	1013	4.82	7	13851	532	5201	745
	MF	3093	162	1020	4.97	6	13914	532	5200	745

Table 6.2 We summarise the 5% percentage of spurious and the 95%/100% completeness of the catalogues at the Planck frequencies. Regarding the percentage of spurious, columns three to seven show the number of detected sources, N_{d_5}, the number of spurious sources N_{sp_5}, the corresponding flux detection limit, S_5, the SNR for S_5 and the average error in the estimation at this flux limit. We allow for a 5% of spurious, where this percentage has been calculated as $N_{sp}/(N_d + N_{sp})$. Regarding the completeness, the flux limits at which the catalogues are complete at the 95% and 100% are shown (columns eigth and ten), and their corresponding number of detections, $N_{d_{95}}$ and $N_{d_{100}}$ (columns nine and eleven).

the probability that two such sources fall inside the same beam is almost negligible. Moreover, at higher Planck frequencies the situation is still better. At 100 GHz we find that at the 5% false detections limit, the average number of sources per beam is ~ 0.0014, whereas for the 857 GHz channel that number decreases to ~ 0.0008 sources per beam. On the other hand, we have to remind that our simulations do not take into account the clustering of sources. If source positions are correlated in the sky – as it is well known for all the source populations observed by Planck – the probability of finding two bright galaxies at the same angular separation in the sky increases. Therefore, with a low-resolution experiment, like Planck, we will observe the summed contribution of groups (or clumps) of sources within the same beam area. The problem has been recently discussed by Negrello et al. [105], who found that, in the presence of strong clustering, source confusion can be important even above the canonical 5σ detection limit, thus modifying source number counts. However, this effect is likely to be important only at Planck HFI frequencies and for the highly clustered high-redshift proto-spheroidal galaxies (see, e.g., the thorough analysis by González-Nuevo et al. [50]). In any case, this study goes beyond the purposes of this work and it shall be tackled in a forthcoming one.

6.5.2 Other compact sources

Other compact but not completely point-like objects will be observed by Planck. The most important among these objects are galaxy clusters observed thanks to the Sunyaev-Zel'dovich (SZ) thermal effect. Detailed simulations of the local universe have shown that the SZ signal from low-redshift clusters and superclusters should be marginally detectable by Planck [39, 63]. On the other hand, very few SZ clusters show angular scales larger than ten arcminutes. Since the scale of these extended clusters is significantly different from the scale of the point sources (i.e., the beam size), the filtering with either a wavelet or a matched filter – both optimised for the scale of the point objects – will tend to cancel the SZ signal just in the same way as it cancels the rest of the diffuse signal and the large scale fluctuations of the background. Therefore, large SZ clusters are not expected to affect significantly the detection process.

Most of the SZ clusters, however, shall be observed as "unresolved" or point-like (i.e., smaller than the Planck beam). In the latter case, they have to be treated in the same way as point sources, except for the fact that their fluxes are typically much fainter. Even the brightest clusters are on the verge of the detectability, given the sensitivities of Planck detectors. As already discussed by many authors, it shall be necessary to combine the signal measured in various frequency channels in order to detect clusters

with Planck [70]. When using a channel-by-channel detection strategy, as the one presented in this work, the impact of SZ clusters is very small. In fact, at $\nu < 217$ GHz, SZ clusters appear as "cold spots" and therefore cannot be detected above any positive flux threshold. At 217 GHz, the thermal SZ effect is zero and the kinematic SZ effect is well below the level of the CMB fluctuations. Above 217 GHz there will be some minor effect due to the thermal SZ effect that may lead to a small number of false detections. The detailed study of this kind of contamination shall be addressed in a future work.

As for Galactic compact sources, representing different evolutionary stages in stellar evolution – i.e., compact pre-stellar cores, young stellar objects and supernova remnants – many of them shall be observed by Planck. Current estimates predict that Planck surveys should detect from many hundreds to thousands of these sources, depending on the subclass (see Table 5.3 in the Planck BlueBook, "The Scientific programme", ESA-SCI(2005)1 [4]. In particular, one of the most relevant classes of Galactic compact sources is that of HII regions, which provide relevant information on early stages of stellar evolution and on the Galactic spiral structure. The thorough analysis made by Paladini et al. [109] has demonstrated that the vast majority ($> 80\%$) of the 1442 HII regions in their Synthetic Catalogue shall be detected by Planck with a very high signal-to-noise ratio ($S/N \geq 100$). In any case, all these sources have well known positions in the sky and, moreover, almost all of them lay at very low Galactic latitude. Therefore, they shall be easily identified and subtracted out. Finally, Planck should also observe 397 asteroids and a significant fraction (50-100 objects) of them with a high S/N ratio [24]. However, these Solar System bodies are moving objects very close to the Earth and, thus, they shall show variable positions and fluxes, depending from their heliocentric and geocentric distances, even during a single Planck scan of 360°.

6.5.3 Systematics

As explained in section 6.3, our simulations can be regarded as "state of the art" as for the realism of the simulations of the physical components (CMB, Galactic foregrounds and extragalactic objects) and we have used the nominal noise levels, beams and pixel sizes of the Planck mission. However, some systematics of relevance have not been included in the simulations. Among them, the ones that can affect our current results are: anisotropic noise, $1/f$ noise, thermal effects and non-symmetric beams.

$1/f$ noise and thermal effects in the electronics of the satellite will lead to large scale noise fluctuations across the sky. Since the filters here discussed operate at small an-

[4] http://www.rssd.esa.int/index.php?project=PLANCK

gular scales, these large scale fluctuations tend to be cancelled out by the filters and should not affect the detection of point sources. Anisotropic noise will appear due to the non-uniform sky coverage of the satellite instruments. Furthermore, mapmaking algorithms can introduce some degree of noise correlation over small angular scales. Non-uniformity of the noise will make easier to detect point sources in some areas of the sky (those that are better scanned) and more difficult to detect in others: on average, the integral number of detections should not change very much. Noise correlation, on the other hand, can be a non negligible effect and it must be studied in a future work. In any case, Vielva et al. [146] have found that their results with the Mexican Hat Wavelet did not vary when anisotropic noise pattern and $1/f$ noise were considered instead of isotropic white noise.

We have worked with idealised beams that are circularly symmetric and Gaussian-shaped. In a real experiment this will not be the case. The real response of the beam shows more complexity, with side lobes, ellipticity and even changing the orientation in the sky of the projected shape. As long as the beam profile is well known, it is straightforward to construct the corresponding MF. Even in the case of non-symmetric beams this can be done, by increasing the computational complexity of the problem. Therefore, when using the MF, real beams can be in principle handled. Regarding the standard Mexican Hat Wavelet, Vielva et al. [146] have tested the influence of realistic asymmetric beams. Those authors have shown that, although the MHW is an isotropic wavelet, it can also be adequate to perform the detection of point sources that show a slight Gaussian asymmetry. This is precisely the situation for the Planck beams (see the Planck BlueBook, ESA-SCI(2005)1). For a more detailed discussion, the reader is referred to Vielva et al. [146].

6.5.4 Extension to the sphere

If we want to extend our work to the sphere, it is important to address the problem of very variable foregrounds from one region of the sky to the other. Then it is necessary to operate locally. From the point of view of implementation, there are two approaches to this problem: to work with small flat patches, as we have done in this work, or to work directly on the sphere using the harmonic transform instead of the Fourier transform, as it was done in Vielva et al. [146]. The first approach is valid if the patches are small enough (no larger than $\sim 15 \times 15$ square degrees), but it implies to project the data from the sphere to the plane and to repixelise the samples (from some non-square pixels on the sphere such as the ones used by HEALPix to the square flat pixels of the patches). This leads to some deformation, especially for the outer parts of the flat

patches and for high latitudes in the sphere. Therefore, the flat patch approach leads to some amount of "systematic" degradation of the data. Besides, in order to cover all the sky it is necessary to decide how to choose the positions of the patches, how much overlapping among the different patches is necessary and how to correct the estimated flux of each source taking into account the deformation just mentioned.

Therefore, in some cases it could be preferable to work directly in the sphere. The most simple way to take into account the variability of the foregrounds is to use the harmonic transform to filter the sphere several times, using each time a filter that is adapted to the statistical properties of a given area of the sky. This is the approach adopted by Vielva et al. [146]. But the number of different filters used should not be very large or the CPU time required would be unreasonably long. Fast harmonic transform algorithms make possible to filter the whole sky in a relatively short time [52], but even so the process can take a significant amount of time for high resolution maps (for example, performing the harmonic transform and calculating the angular power spectrum of a NSIDE=2048 HEALPix map takes 108 minutes in a 3 GHz Intel Pentium processor). Thus, it is necessary to reach a compromise between acting locally (that may require to filter the data many times) and saving CPU time.

In the case of wavelets it has been successfully shown [146] that it is possible to estimate locally the optimal scale of all the regions, group together different regions with similar optimal scales and construct a small number (around fifteen in the worst case) of filters on the sphere for these optimal scales. In their study it was possible to reduce the number of times it was necessary to filter the maps due to the fact that the functional form of the wavelets depend only on one parameter (the optimal scale) that varies slowly across large zones of the sky and it is easy to group the optimal scales in a small number of bins without loosing much efficiency. Even so, their algorithm takes ~ 72 hours for the most CPU time-demanding channel (857 GHz) in a Compaq HPC320 (Alpha EV68 1-GHz processor) and requires 4 GB of RAM memory, a non-negligible amount of computer resources.

On the contrary, the MF functional form depends on the power spectrum of the data. The shape of the local power spectrum varies wildly from one region of the sky to other, and it is not easy to group local power spectra in classes to reduce the number of times the sky must be filtered. A taxonomic criterion to group power spectrum curves should be provided, introducing a new arbitrarity in the process. If one wants to skip this arbitrarity, it is necessary to construct one filter *for every region of the sky and to filter the sky map a large number of times*, especially for high resolutions. Nowadays, this process requires a huge amount of computational resources. This gives another reason

to prefer wavelets to MF when working in the sphere.

6.6 Conclusions

We have compared the performance of three filters when dealing with the detection of point sources in CMB flat sky maps. These filters are the well known MF, the Mexican Hat Wavelet (MHW1) and the recently introduced Mexican Hat Wavelet 2 (MHW2). The latter is the second member of the so-called Mexican Hat Wavelet Family (the MHW1 is the first), a group of wavelets obtained by applying the Laplacian operator to the Gaussian [51]. This new wavelet is part of an effort to improve the MHW1, a tool already exploited by our group that has proved very useful in the detection of compact sources and of non-Gaussianity in CMB maps [144, 146, 147].

We have tested these tools in realistic 2D simulations of the microwave sky prepared in the framework of optimising the efficiency in separating the various astrophysical components in the forthcoming ESA's Planck Satellite all-sky maps. As for the Galactic foregrounds and the S-Z effect in clusters of galaxies, we have used the available "Planck Reference Sky Model"; we have adopted the Standard "concordance" Model for simulating CMB anisotropy maps and, as for extragalactic point sources, we have used simulations obtained by the software discussed in González-Nuevo et al. [50] and with the number count models for sources of De Zotti et al. [32], Granato et al. [53, 54] and Negrello et al. [104]. We then applied the three considered filters to a sufficient number of flat patches to cover half of the sky (2π sr, $b > |30^\circ|$) (see Section 3).

We have found that the MHW2 and the MF outperform the MHW1 in some aspects, especially at the lowest Planck frequencies. The three filters yield approximately the same number of real detections, down to the same flux detection limit, although the MHW1 yields a corresponding higher number of spurious detections. Moreover, the MHW2 and the MF give comparable results for almost every one of the analysed indicators. As shown in Figure 6.1, it is remarkable that, even the estimated shape of the MF tends to that of the MHW2, at its optimal scale, for most of the frequencies discussed in this work.

In a previous work [146], a multi-fit approximation to estimate the flux density of the sources detected by the MHW1 was shown to be able to improve the results (as compared with the direct approach used in this work). We have applied this technique to the simulated maps used in this work and we found different results for the LFI and the HFI Planck frequency channels. In the first case, LFI, the improvement is small and the final results are never comparable to the ones obtained with the MHW2. In the second

case, this procedure helps to slightly reduce the number of spurious sources, except for the highest frequency of HFI (857 GHz), where the decrease in the number of spurious is significant and the MHW1 approaches the results obtained with MHW2.

These results are very important because both wavelets, the MHW1 and the MHW2, are represented by a known analytical function. The only parameter that needs to be obtained for each simulation is the "optimal scale", which is calculated locally in a very easy way. On the other hand, the correct definition of the MF implies a number of steps. Firstly, it is necessary to estimate the value of the power spectrum for all the Fourier modes present in the image, especially for the low modes where the power spectrum is *noisy*. Secondly, the use of such a noisy power spectrum to construct the MF often yields a filter with many discontinuities in Fourier space which, in turn, produces ringing effects in the filtered image. Therefore some smoothing in the spectra needs to be done before constructing the filter, which introduces further arbitrariness. Thirdly, sometimes it will not be possible to properly estimate some Fourier modes, for example when using masks with missing data, and these modes will have to be guessed.

Therefore, the most relevant conclusion of this analysis is that the MHW2 can be surely a better choice for the definition of a blind source catalogue – like the ERCSC foreseen for the future Planck mission – because it gives numbers of detected and of spurious sources comparable to the ones obtained with the MF but is easier to implement, more robust and has much lesser CPU requirements, especially in all-sphere applications.

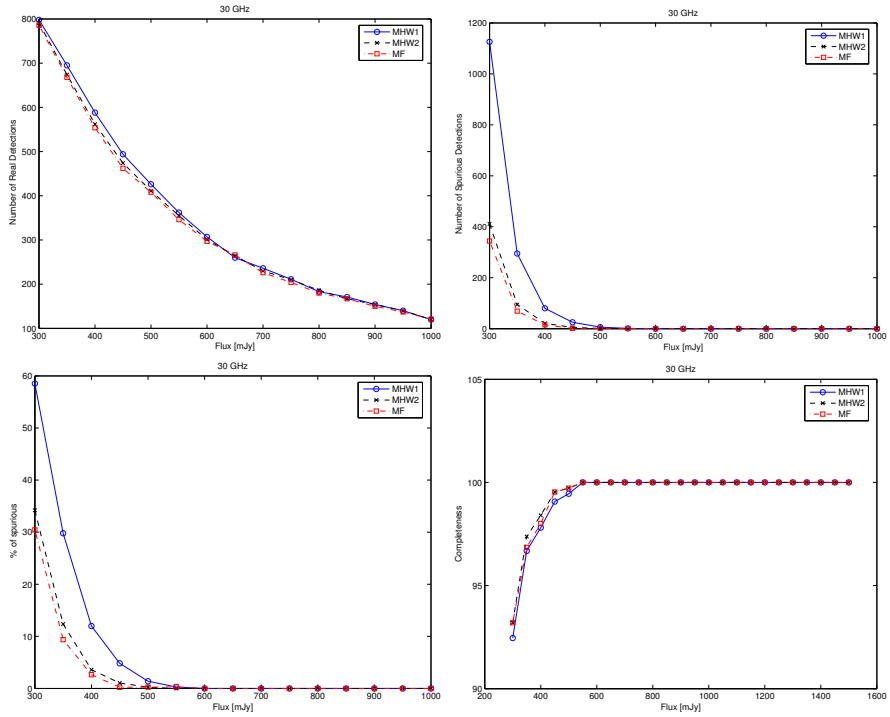

Figure 6.4 30 GHz. In this figure we compare the results obtained for the three considered filters, the MHW1 and MHW2 at their optimal scales and the MF. In the upper left figure we show the number of detected sources above a given flux detection limit. In the upper right figure we present the number of spurious or false detections above a given flux detection limit. The lower left figure shows the percentage of spurious sources (defined as the number of spurious divided by the sum of spurious and real detections) above a given flux detection limit. The lower right figure shows the completeness level of the catalogues above a given flux detection limit. The solid line corresponds to the MHW1, the dashed line corresponds to the MHW2 and the dot-dashed line corresponds to the MF. Similarly, the circle, cross and squares correspond to the MHW, MHW2 and the MF respectively.

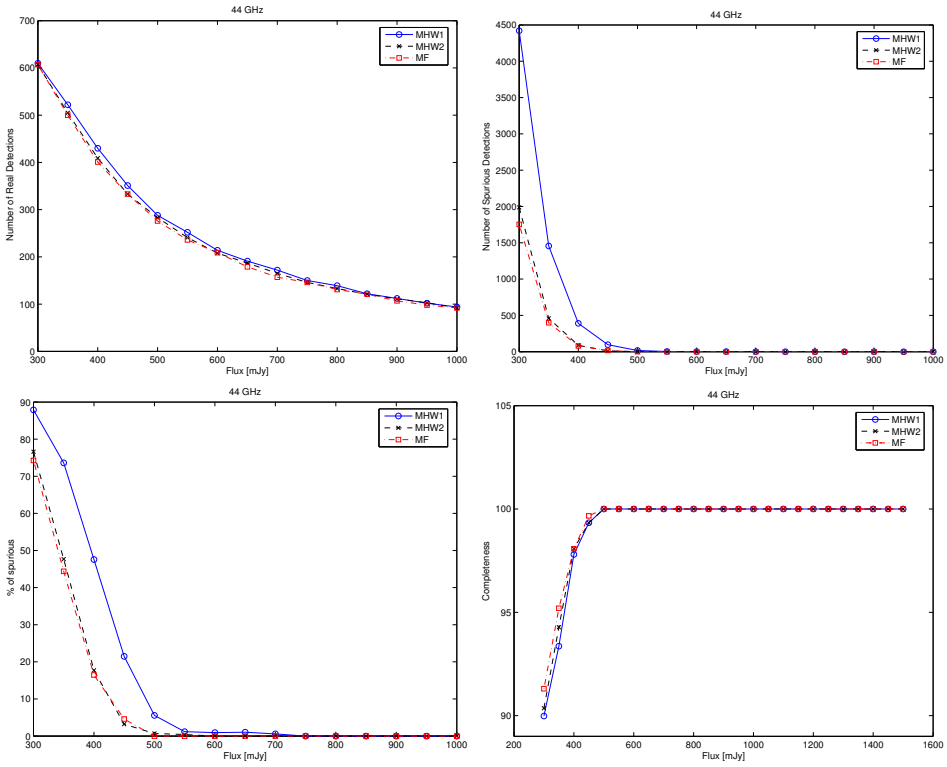

Figure 6.5 The same as in Figure 6.4 but at 44 GHz.

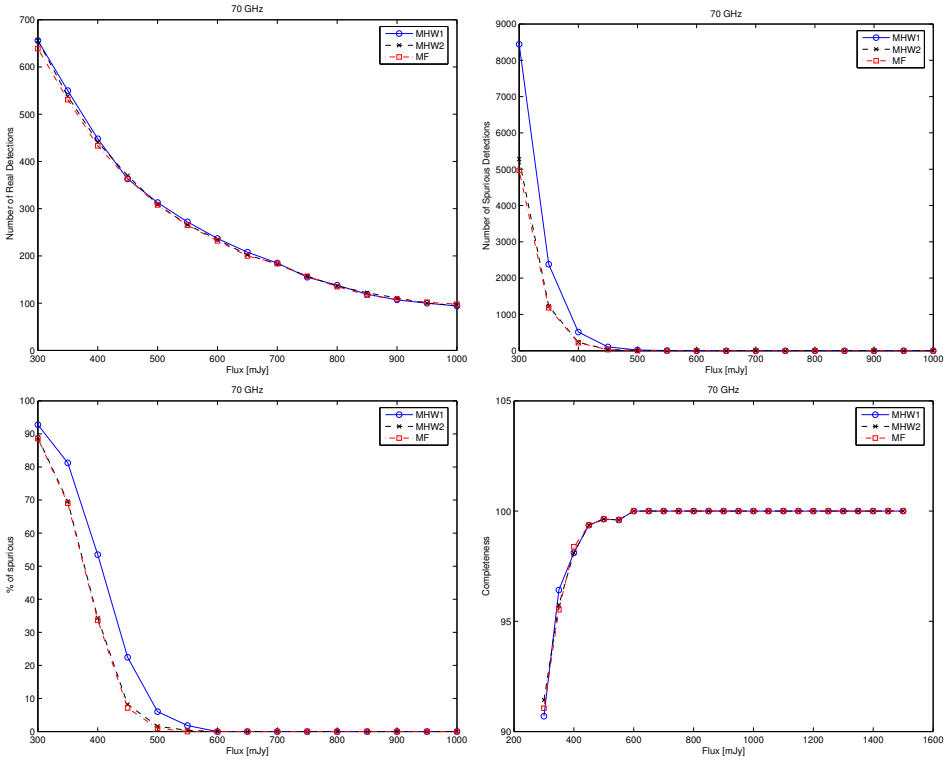

Figure 6.6 The same as in Figure 6.4 but at 70 GHz.

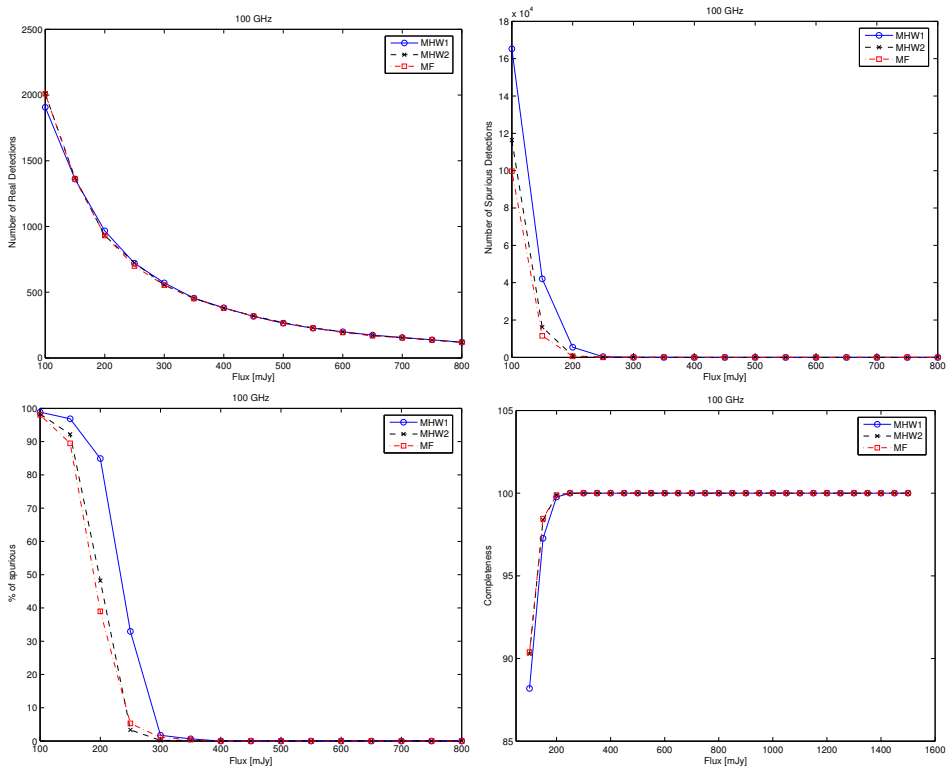

Figure 6.7 The same as in Figure 6.4 but at 100 GHz.

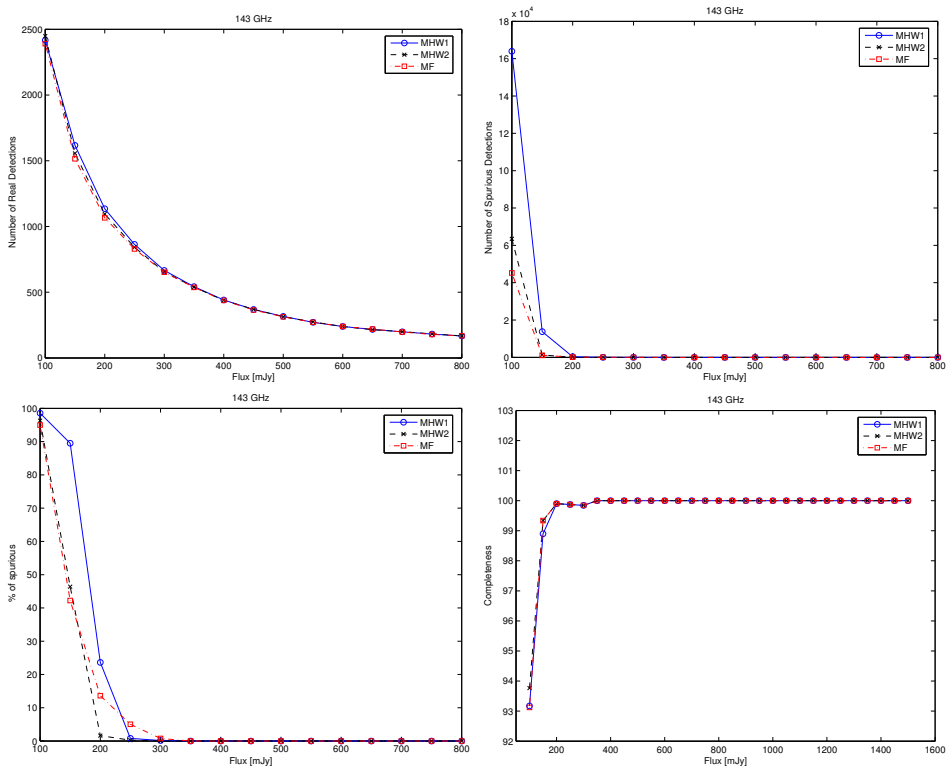

Figure 6.8 The same as in Figure 6.4 but at 143 GHz.

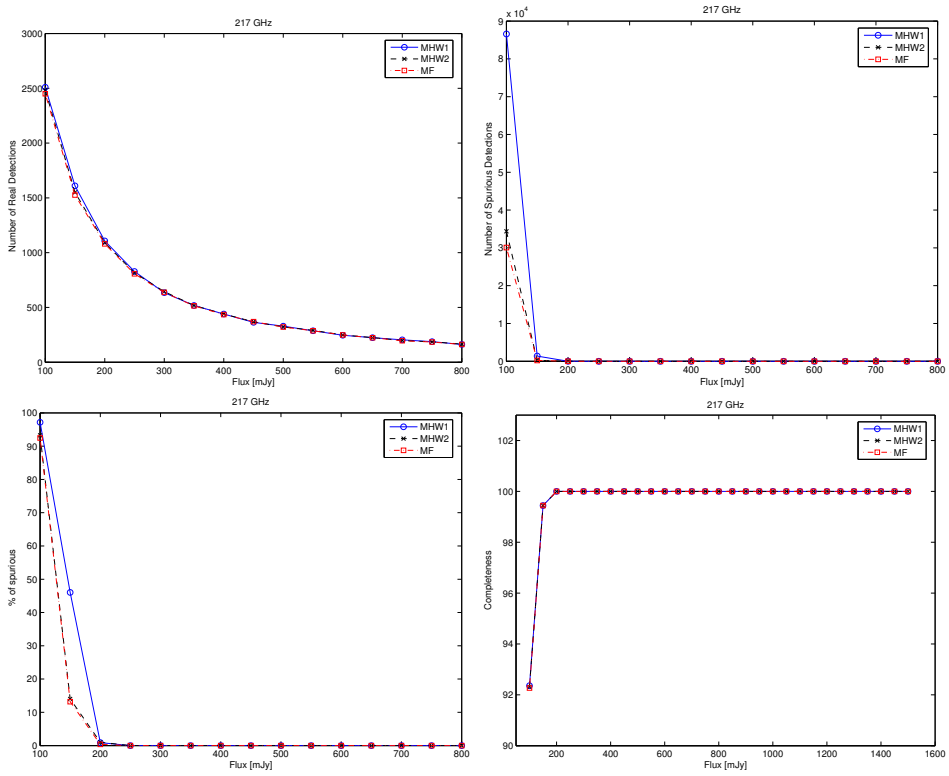

Figure 6.9 The same as in Figure 6.4 but at 217 GHz.

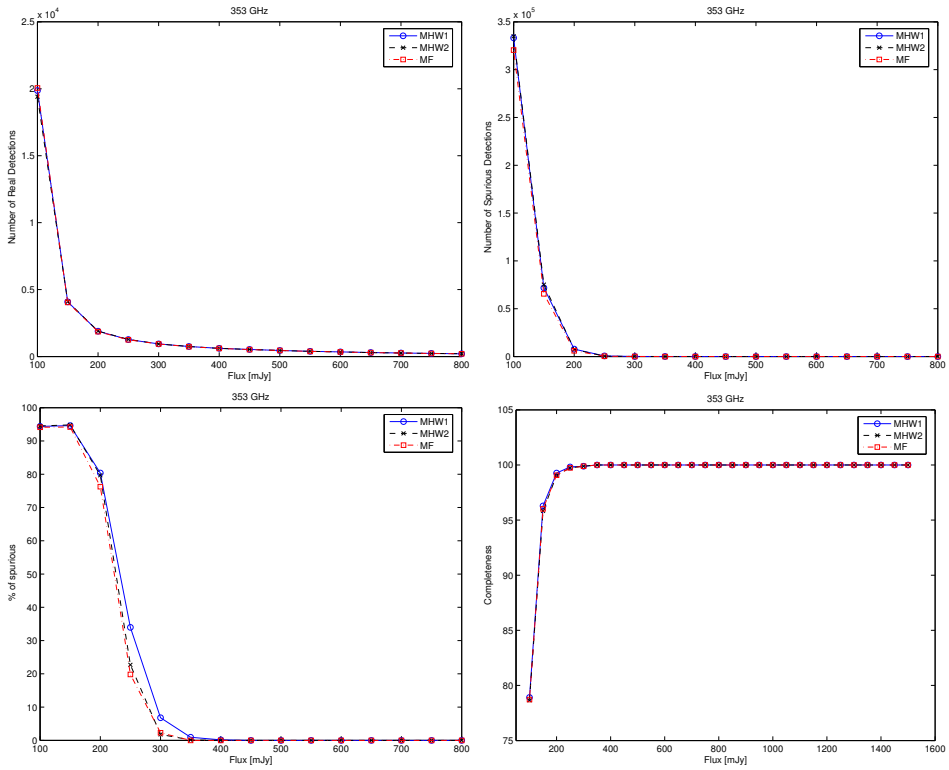

Figure 6.10 The same as in Figure 6.4 but at 353 GHz.

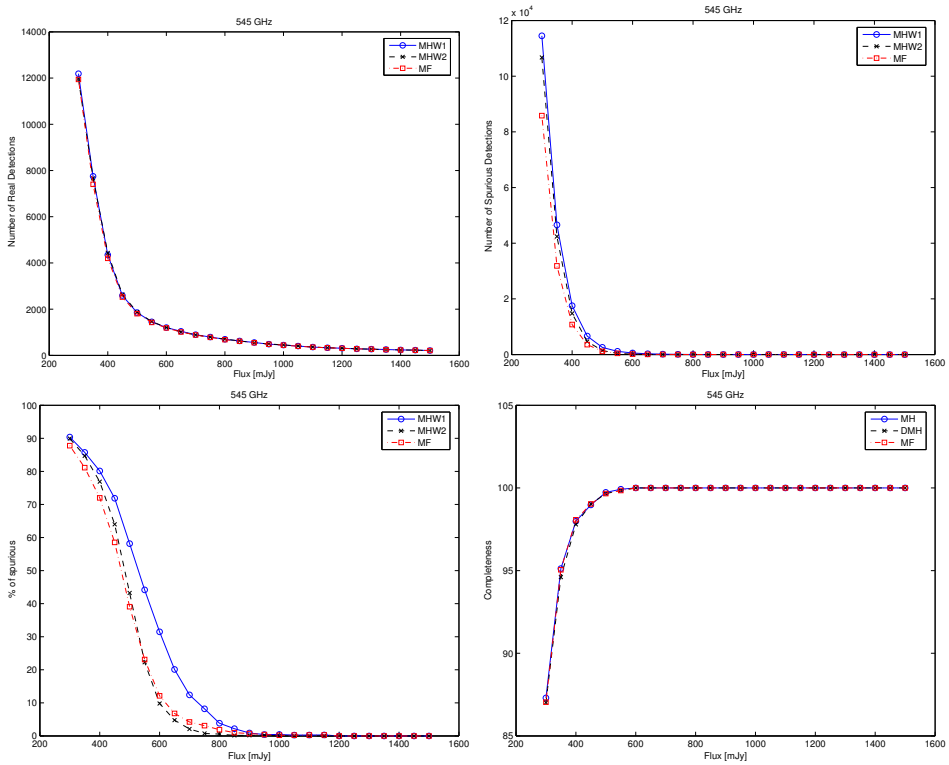

Figure 6.11 The same as in Figure 6.4 but at 545 GHz.

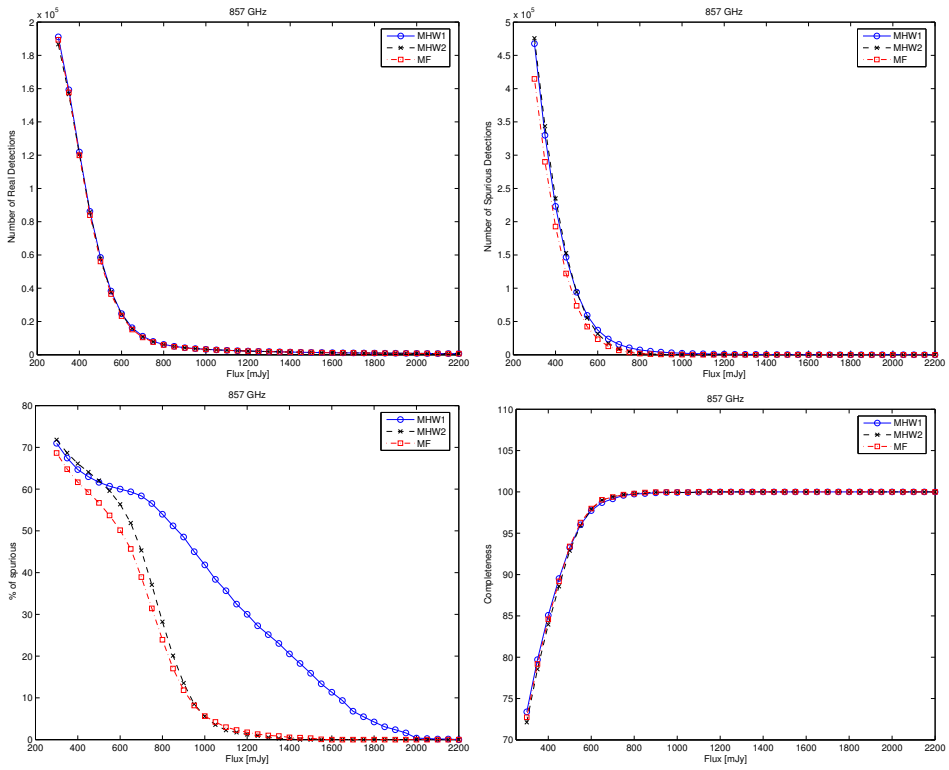

Figure 6.12 The same as in Figure 6.4 but at 857 GHz.

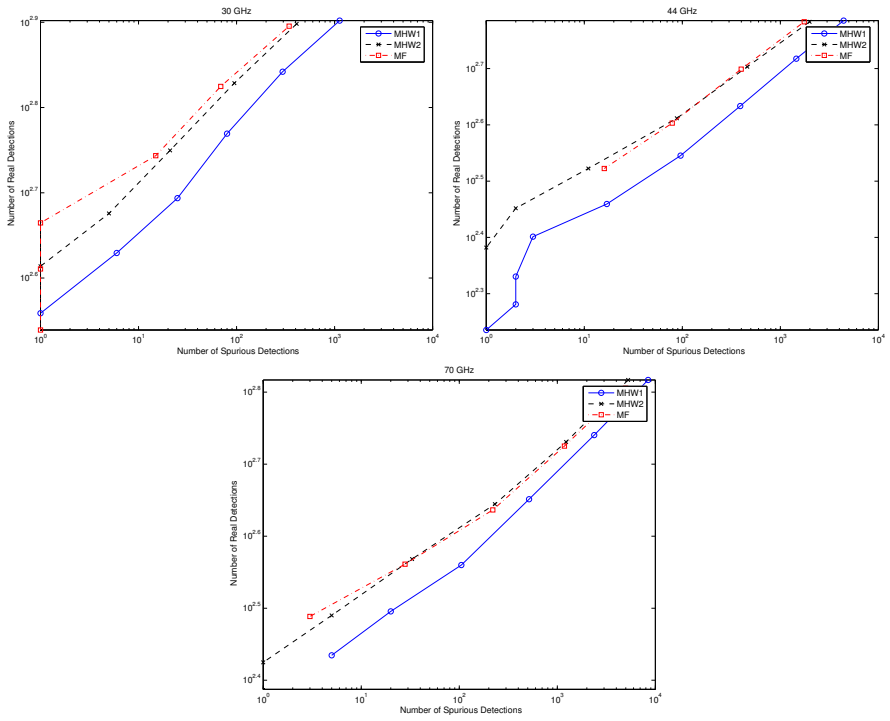

Figure 6.13 For the Planck LFI channels, 30, 44 and 70 GHz, we show the number of spurious detections vs. the number of real detections for all the Planck frequency channels. This plot is very useful for comparing the performance of the chosen filters.

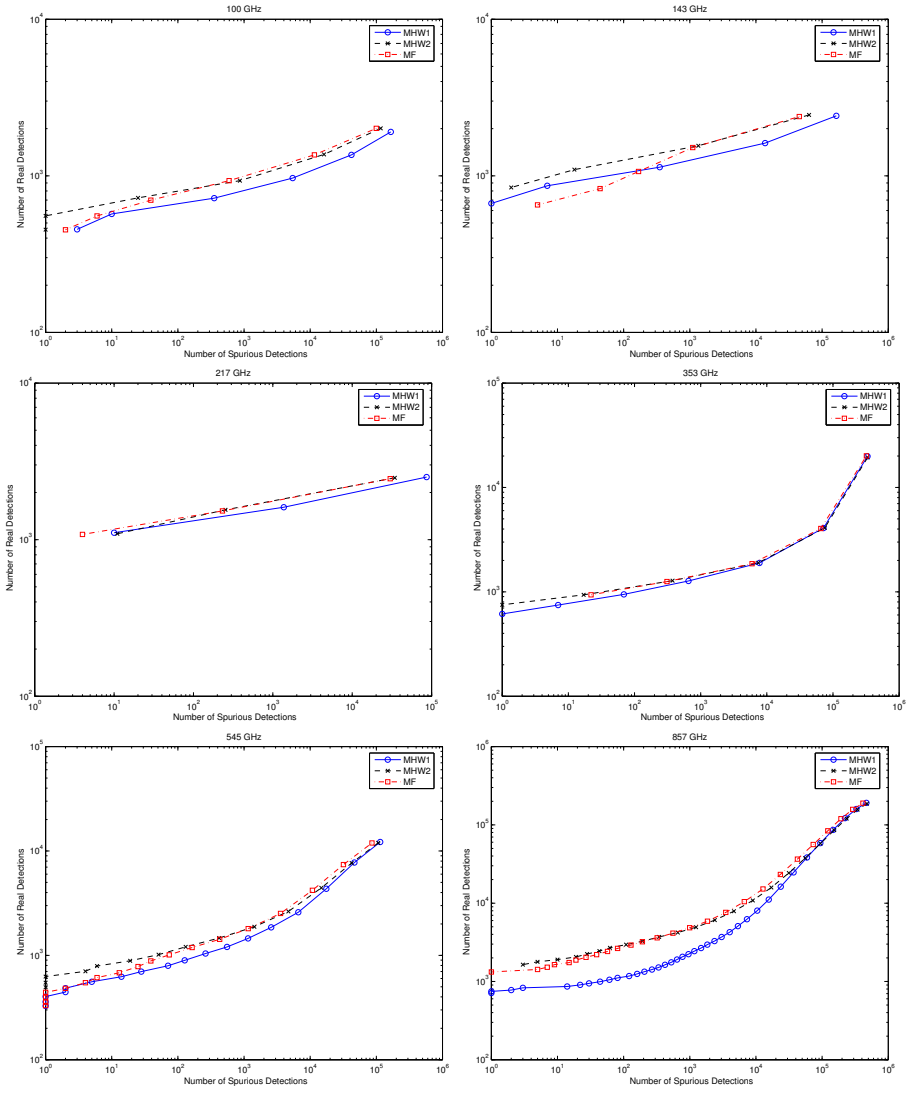

Figure 6.14 For the Planck HFI channels, 100, 143, 217, 353, 545 and 857 GHz, we show the number of spurious detections vs. the number of real detections for all the Planck frequency channels. This plot is very useful for comparing the performance of the chosen filters.

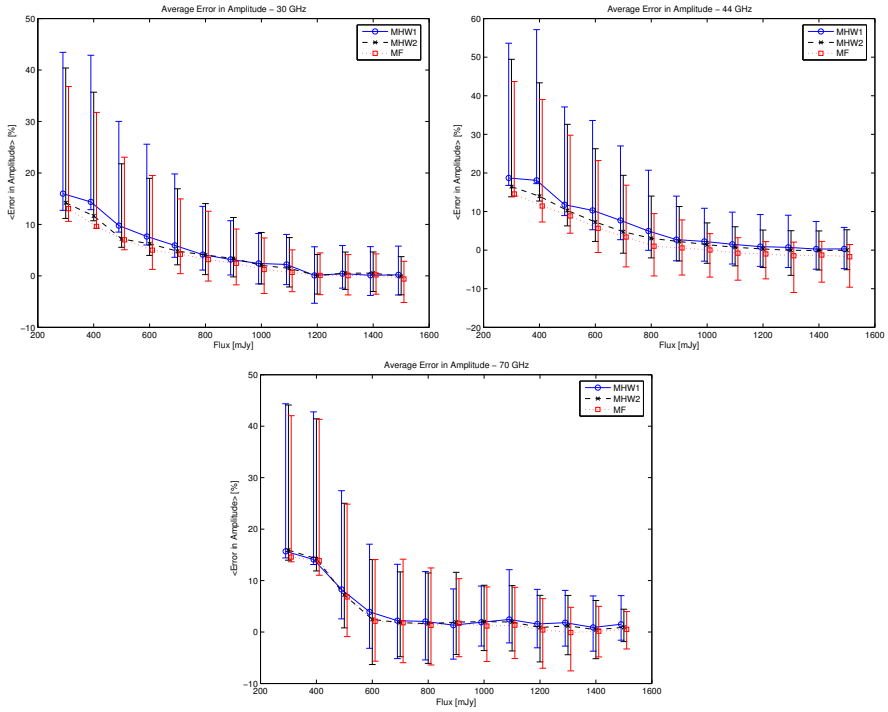

Figure 6.15 For the Planck LFI channels, 30, 44 and 70 GHz, we show the average error (68% error bars) in the estimated flux density for all the sources observed above different flux detection limits. The error is defined as $(< A_{est} - A_{real})/A_{real} >$, where A_{est} is the estimation of the flux in the simulated patch after filtering and A_{real} is the flux of the source in the catalogue. For the sake of clarity, we have plotted the errorbars with an offset of 10 mJy in the x-axis.

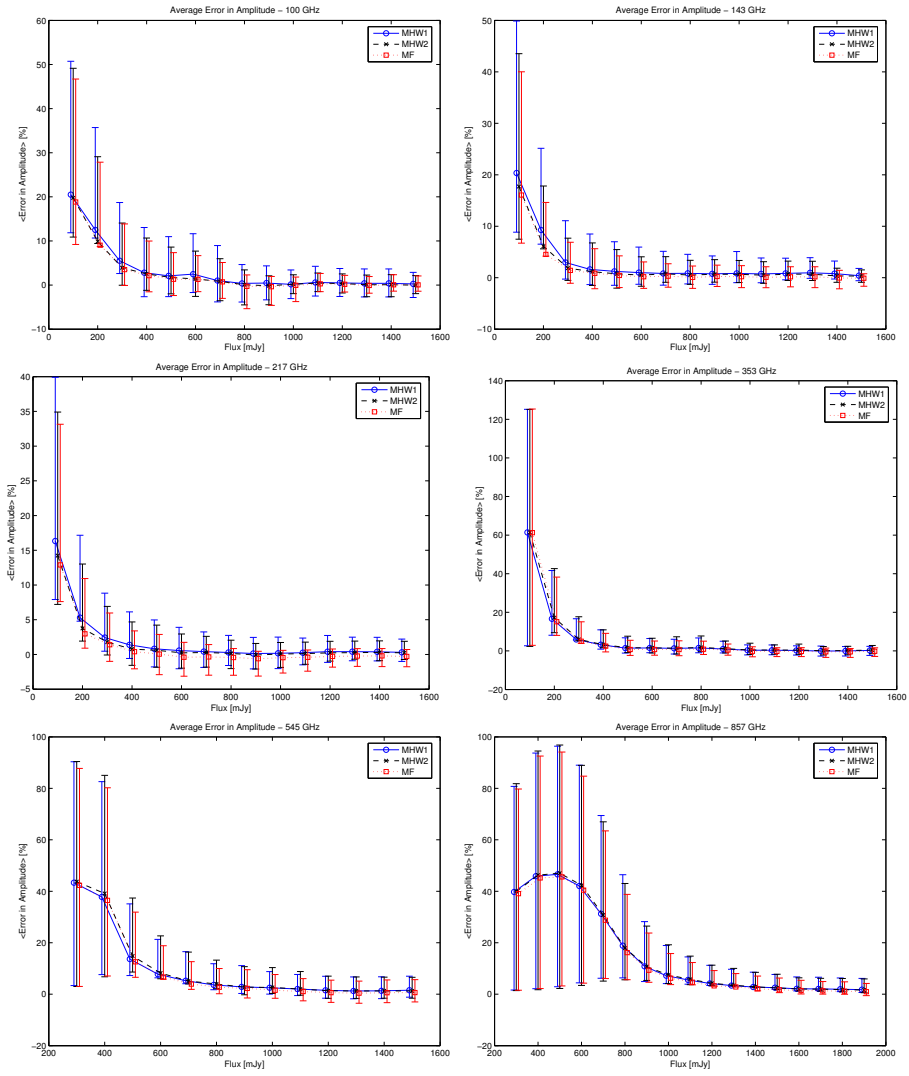

Figure 6.16 For the Planck HFI channels, 100, 143, 217, 353, 545 and 857 GHz, we show the average error (68% error bars) in the estimated flux density for all the sources observed above different flux detection limits. The error is defined as $(< A_{est} - A_{real})/A_{real} >$, where A_{est} is the estimation of the flux in the simulated patch after filtering and A_{real} is the flux of the source in the catalogue. For the sake of clarity, we have plotted the errorbars with an offset of 10 mJy in the x-axis.

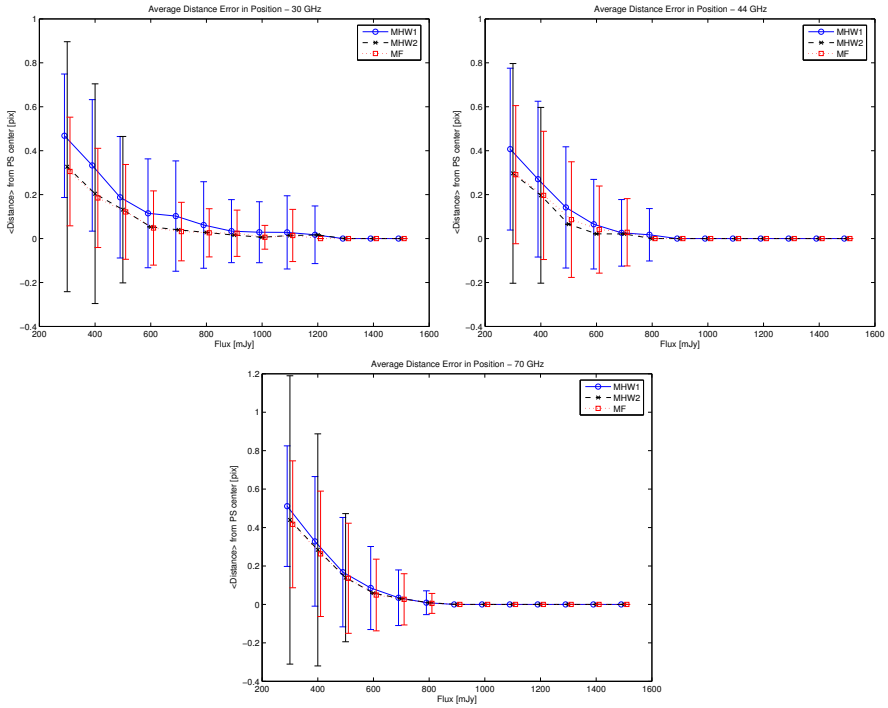

Figure 6.17 For the Planck LFI channels, 30, 44 and 70 GHz, we show in each panel and for different flux detection limits, the average distance between the center coordinates of the detected source with respect to the actual coordinates of the corresponding simulated source in the input catalogue. For the sake of clarity, we have plotted the errorbars with an offset of 10 mJy in the x-axis.

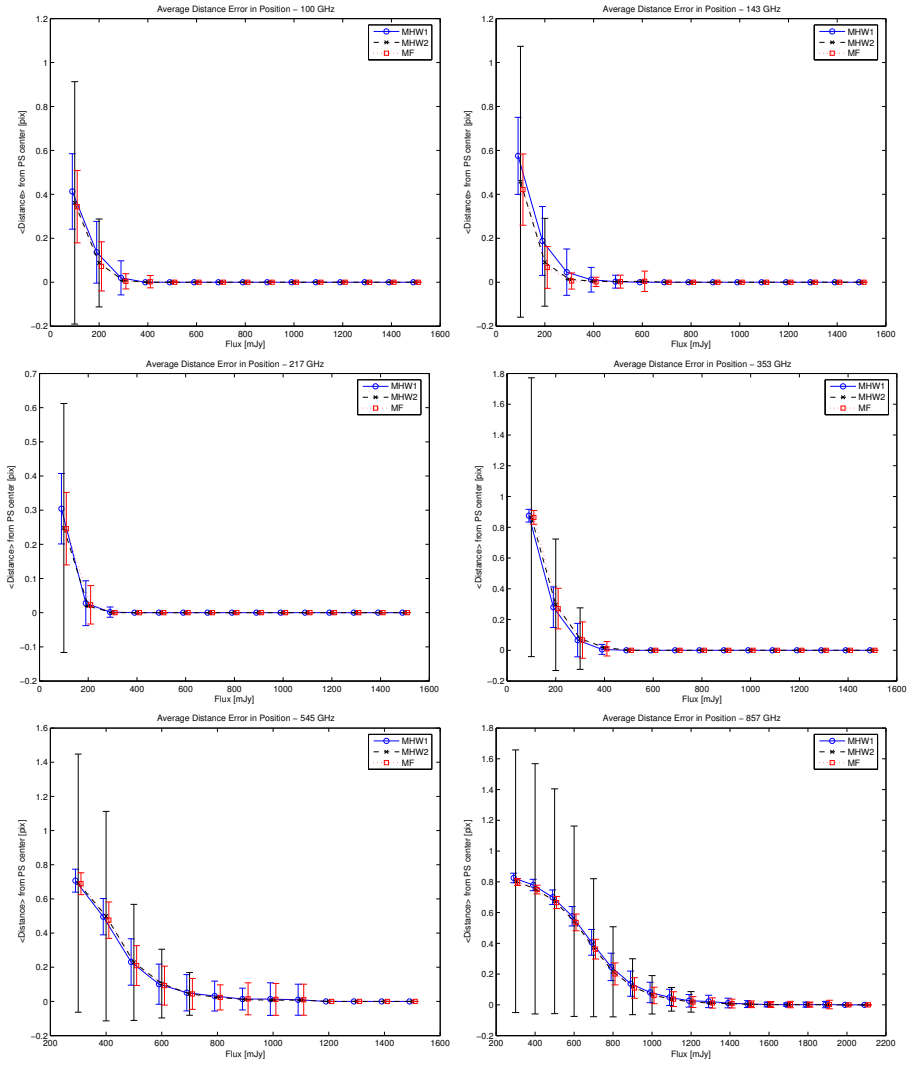

Figure 6.18 For the Planck HFI channels, 100, 143, 217, 353, 545 and 857 GHz, we show in each panel and for different flux detection limits, the average distance between the center coordinates of the detected source with respect to the actual coordinates of the corresponding simulated source in the input catalogue. For the sake of clarity, we have plotted the errorbars with an offset of 10 mJy in the x-axis.